VIP Lithium-Ion Batteries Very Important Paper

International Edition: DOI: 10.1002/anie.201500677
German Edition: DOI: 10.1002/ange.201500677

Solvated Graphene Frameworks as High-Performance Anodes for Lithium-Ion Batteries**

*Yuxi Xu, Zhaoyang Lin, Xing Zhong, Ben Papandrea, Yu Huang, and Xiangfeng Duan**

Abstract: *A solvent-exchange approach for the preparation of solvated graphene frameworks as high-performance anode materials for lithium-ion batteries is reported. The mechanically strong graphene frameworks exhibit unique hierarchical solvated porous networks and can be directly used as electrodes with a significantly improved electrochemical performance compared to unsolvated graphene frameworks, including very high reversible capacities, excellent rate capabilities, and superior cycling stabilities.*

Electrochemical energy storage has become a key enabling technology for sustainable, clean, and efficient energy supply. In this regard, lithium-ion batteries (LIBs) with high energy and power densities are highly desired devices for advanced portable electronic devices and electric vehicles.[1–3] The electrode materials are the central components of LIBs and largely dictate their ultimate performance. Although graphite has been widely used as an anode material in current commercial LIBs, its low theoretical capacity (372 $mAh\,g^{-1}$) and poor rate capability cannot meet the increasing requirements for next-generation LIBs. Graphene, a single-atom-thick two-dimensional carbon lattice, has been considered as a promising alternative electrode material for LIBs owing to its superior intrinsic electrical conductivity, high specific surface area, excellent mechanical flexibility, and broad electrochemical window.[4–6] However, the strong van der Waals and π–π stacking interactions between graphene sheets make them readily aggregate to form graphite-like powders or films with dense layered microstructures when they are processed into bulk electrode materials, leading to a severely decreased surface area and much higher Li ion diffusion resistance and therefore inefficient utilization of the graphene layers for Li storage.[7–10] Furthermore, polymer binders and/or conductive additives are generally indispensable, which increases not only the complexity of electrode preparation but also the weight of the passive components and imposes an adverse effect on the electrochemical performance.

Monolithic graphene frameworks with three-dimensional (3D) interconnected porous networks in the form of hydrogels, aerogels, or foams have recently received intense interest as electrochemical energy storage devices because of their large specific surface area, multidimensional continuous electron-transport pathways, and rapid ion-diffusion characteristics as well as excellent mechanical strength.[11–18] Taking advantage of these desirable features of graphene frameworks, considerable efforts have been focused on the incorporation of various nanostructured transition-metal oxides and sulfides into the graphene frameworks to prepare 3D hybrids that efficiently combine the advantages of both components and show high reversible capacities, fast charge/discharge rates, and good cycle performances when employed as anode materials for LIBs.[19–35] However, previous studies of 3D graphene hybrids have largely been limited to graphene aerogels that were prepared by freeze-drying of the hydrogel precursor, which is expected to disturb the pristine microstructure of the graphene frameworks and thus prevent achieving the full potential of 3D graphene. A fundamental understanding of how the graphene framework functions as an anode material is urgently needed for the further development of 3D graphene materials for advanced LIBs.

Herein, we report, for the first time, the preparation of solvated graphene frameworks (SGFs) through a convenient solvent-exchange approach for high-performance anodes in LIBs. The mechanically strong SGFs can be used directly as electrodes without adding any other binders or conductive additives and deliver a very high reversible capacity of 1158 $mAh\,g^{-1}$ at a charge/discharge rate of 0.1 $A\,g^{-1}$, which is 2.6 times higher than that of unsolvated graphene frameworks (439 $mAh\,g^{-1}$). Moreover, the SGFs show excellent rate capabilities with a significant capacity of 472 $mAh\,g^{-1}$ at a high charge/discharge rate of 5.0 $A\,g^{-1}$ and superior cycling stabilities with a capacity retention of 93% over 500 charge/discharge cycles at 5.0 $A\,g^{-1}$. The electrochemical performance of the SGFs is comparable to that of the best graphene-based anode materials that have been reported thus far, and could be largely attributed to the unique solvated porous network of the SGFs, which leads to a higher specific surface area and faster Li ion diffusion than in the unsolvated graphene frameworks used before.

To prepare the SGFs, we first synthesized free-standing graphene hydrogels (GHs) using a modified hydrothermal self-assembly method (Figure 1a, left). After freeze-drying, we obtained graphene aerogels (GAs), which showed little change in shape and size compared to the GHs (Figure 1a,

[*] Dr. Y. X. Xu, Z. Y. Lin, Dr. X. Zhong, B. Papandrea, X. F. Duan
Department of Chemistry and Biochemistry
University of California, Los Angeles
California 90095 (USA)
E-mail: xduan@chem.ucla.edu
Prof. Y. Huang
Department of Materials Science and Engineering
University of California, Los Angeles
California 90095 (USA)

[**] We acknowledge the Electron Imaging Center for Nanomachines (EICN) at the California NanoSystems Institute for technical support of the TEM measurements. X.F.D. acknowledges partial support by a Dupont Young Prof. Award (electrochemical characterization).

Supporting information for this article is available on the WWW under http://dx.doi.org/10.1002/anie.201500677.

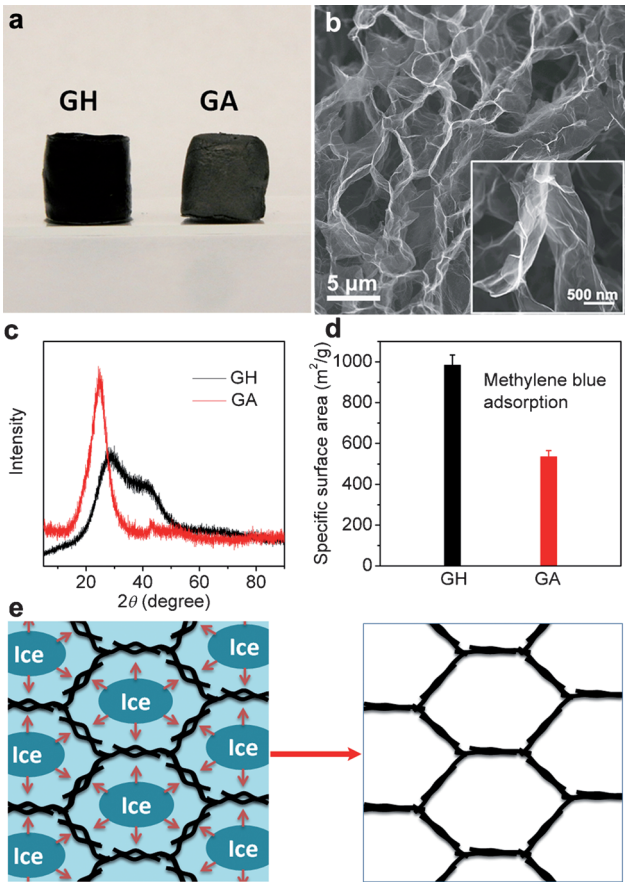

Figure 1. a) Photographs of GH and GA. b) SEM images of the interior microstructures of GA with a high-magnification image shown in the inset. c) XRD patterns of GH and GA. d) Specific surface areas of GH and GA determined by the MB adsorption method. e) Schematic representation of the structural evolution of GH upon freeze-drying.

right). Scanning electron microscopy (SEM) images revealed that the GAs had an interconnected porous network with pore sizes ranging from less than one micrometer to several micrometers and pore walls consisting of thin layers of stacked graphene sheets, which arise from the 3D self-assembly of graphene (Figure 1b).[14] Raman and X-ray photoelectron spectroscopy as well as transmission electron microscopy (TEM) studies confirmed the efficient reduction of graphene oxide (GO) during the synthesis of GH (Supporting Information, Figure S1). Although there was no obvious difference in the appearance of GH and GA, the X-ray diffraction (XRD) patterns exhibited a remarkable difference (Figure 1c). The GA showed a diffraction peak at approximately 25°, which corresponds to a d spacing of 0.36 nm, which is slightly larger than that of graphite (0.33 nm) owing to the existence of residual oxygen functional groups on reduced GO.[36] In contrast, the GH gave no prominent peak at this angle but showed much broader diffraction peaks ranging from approximately 20° to 50°, indicating that the ordering of graphene sheets along their stacking direction is worse in GH than in GA, which is likely due to the water molecules confined within the pore walls of GH.[37,38] This result also suggests that the pore walls of GH are composed of a few layers of stacked graphene sheets, which is consistent with the TEM studies (Figure S1c).

To further probe the difference between the microstructures inside GH and GA, we employed the methylene blue (MB) dye adsorption method to measure the specific surface areas of both samples. In contrast to the frequently used gas adsorption and desorption method, this approach could be used under the pristine wet conditions of the GH to determine its intrinsic specific surface area.[39] Surprisingly, the GH showed a high specific surface area of approximately 980 $m^2 g^{-1}$, which is about 1.8 times larger than that of GA (ca. 530 $m^2 g^{-1}$; Figure 1d). Together, these studies suggest that the face-to-face stacking of reduced GO sheets in the pore walls of GH is much less tight than the stacking of pristine graphene in graphite owing to the flexible corrugated structure and colloidal interactions between hydrated reduced GO sheets containing oxygen functional groups, thus creating abundant micro- and mesopores within the pore walls of GH, which are filled by water molecules and accessible to the MB molecules.[37,38] Upon freeze-drying, a significant portion of the pores within the pore walls of GH were compressed by the gradual growth of ice crystals and the removal of water (Figure 1e), resulting in stronger stacking of reduced GO within the pore walls and a lower specific surface area in the GAs, although some micro- and mesoporosity survived (Figure S2). Furthermore, the macroporous network built by the pore walls can be retained after freeze-drying, and thus no obvious appearance change between GH and GA was observed.

The hydrated GHs could allow for the one-step direct exchange of their interior water molecules with hydrophilic organic solvents, such as ionic liquids (ILs), ethanol, ethylene carbonate (EC), and dimethylformamide (DMF), to prepare a variety of SGFs (Figure 2a). In fact, the GHs are also a kind of SGF but here we use different terms to describe these two materials for reasons of clarity. Even for water-insoluble diethyl carbonate (DEC), we could follow a two-step procedure with ethanol and DEC as the successive exchange solvents to prepare a SGF fully infiltrated with DEC (Figure 2a). Although the XRD patterns of the SGFs showed a peak shift compared to GH, which is probably due to the different solvation effects on the reduced GO sheets, similarly broad diffraction peaks were observed, indicating that the unique stacking structure of the reduced GO and the hierarchical porosity in GH were largely retained in the SGFs (Figure 2b), which is particularly important to extend the function of SGFs for various applications.

To study the electrochemical performance of SGFs as anode materials in LIBs, we used the solvent-exchange method to prepare SGFs infiltrated with 1M $LiPF_6$ in EC/DEC electrolyte. A piece of approximately 2 mm thick mechanically strong SGF was pressed on copper foil to form an approximately 30 μm thick SGF film, which was directly used as the electrode without any other additives or further impregnation with electrolyte to assemble the cells (Figure 3a). The pressed SGF film with a graphene packing density of 0.65 $g cm^{-3}$ showed a high electrical conductivity of approximately 950 $S m^{-1}$. XRD studies of the SGFs before and after pressing (Figure S3) showed similar diffraction peak

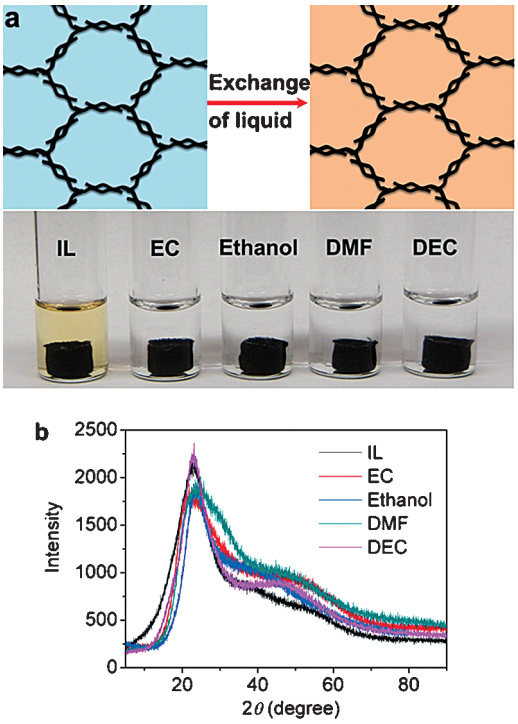

Figure 2. a) Schematic representation of solvent exchange for the preparation of SGFs (top) and photographs of SGFs in various organic solvents (bottom). b) XRD patterns of SGFs.

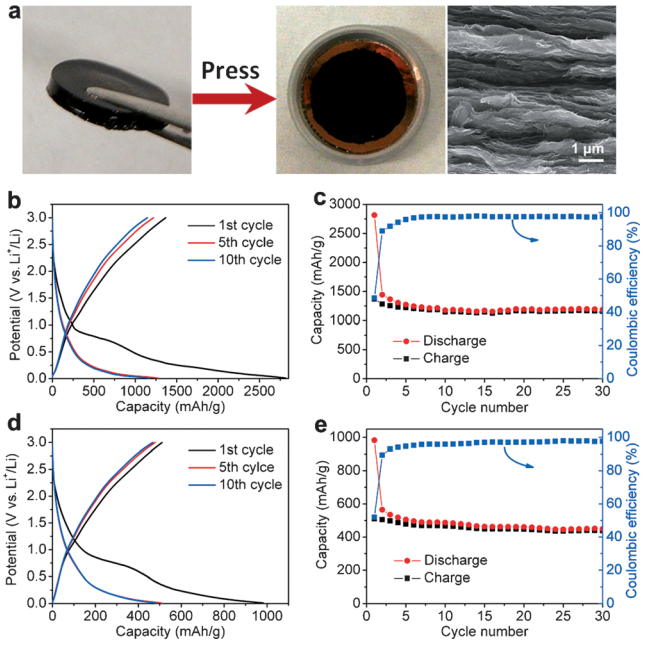

Figure 3. a) Preparation of a binder-free SGF electrode. A piece of SGF (left), its pressed-film electrode on copper foil placed in a coin cell case (middle), and SEM image of the cross-section of the pressed SGF film (right). b) Galvanostatic charge/discharge profiles and c) cycle performance and Coulombic efficiency of the SGF electrode at a low current density of 0.1 $A g^{-1}$ between 3.0 and 0.01 V versus Li^+/Li. d) Galvanostatic charge/discharge profiles and e) cycle performance and Coulombic efficiency of the GA electrode at a low current density of 0.1 $A g^{-1}$ between 3.0 and 0.01 V versus Li^+/Li.

widths and intensities, suggesting that little re-stacking of the graphene sheets had occurred, and that the unique solvated porous network was largely maintained in the pressed SGF film owing to the robust interlock of graphene sheets in the SGF. For comparison, the GA was also tested under the same conditions as an unsolvated graphene framework. Figure 3b–e shows the galvanostatic charge/discharge profiles of SGF and GA electrodes at a current density of 0.1 $A g^{-1}$ within a cutoff voltage window of 0.01–3.0 V versus Li^+/Li. The SGF electrode delivered a specific capacity of 2815 $mAh g^{-1}$ in the initial discharging process and a reversible capacity of 1367 $mAh g^{-1}$ in the first charging cycle with a Coulombic efficiency of 48.5%. The presence of a plateau at approximately 0.8 V and the irreversible capacity loss in the first cycle could be associated with electrolyte decomposition and the formation of a solid–electrolyte interphase (SEI) on the electrode surface (Figure 3b).[7–10] The capacity of the SGF electrode became stable after five charge/discharge cycles. The SGF electrode exhibited a high reversible capacity of 1158 $mAh g^{-1}$ after 30 cycles with a high capacity retention of 85% (Figure 3c). In contrast, the GA electrode showed much lower reversible capacities of 510 and 439 $mAh g^{-1}$ in the first cycle and after 30 cycles, respectively (Figure 3d,e).

The rate performances of the SGF and GA electrodes at different current densities were further studied (Figure 4). At a current density of 0.2 $A g^{-1}$, the SGF electrode could be reversibly charged to 1066 $mAh g^{-1}$ in the fifth cycle, which is much higher than the value for the GA electrode (397 $mAh g^{-1}$). When the current density was increased to 0.5, 1.0, and 2.0 $A g^{-1}$, the SGF electrode could deliver reversible capacities of 875, 749, and 626 $mAh g^{-1}$, respectively. More importantly, even at a very high current density of 5.0 $A g^{-1}$, a stable reversible capacity of 472 $mAh g^{-1}$ could still be achieved for the SGF electrode, which is 3.7 times higher than that of the GA electrode (101 $mAh g^{-1}$). Particularly, when the current density was returned to the initial 0.2 $A g^{-1}$, a reversible capacity of 1034 $mAh g^{-1}$ could be recovered (Figure 4c). Moreover, the kinetic features of the charge/discharge curves at high current densities were similar to those at low current densities (Figure 4a). For graphene electrode materials, the capacity below 0.5 V (vs. Li^+/Li) comes from lithium intercalation into the graphene layers, whereas the capacity above 0.5 V (vs. Li^+/Li) is mainly associated with the Faradic capacitance on the surface or edge sites of the graphene sheets.[7] Therefore, for the SGF electrode, the capacities arising from lithium intercalation are approximately 903 and 322 $mAh g^{-1}$ at 0.1 and 5.0 $A g^{-1}$, respectively, contributing as much as approximately 78% and 68% of the total capacity of the SGF electrode, respectively, which is significantly more than the values achieved with the GA electrode (ca. 70 and 51% at 0.1 and 5.0 $A g^{-1}$, respectively), especially at a high current density. These results suggest that the SGF electrode has more favorable charge transport and ion diffusion processes than the GA electrode, which was confirmed by electrochemical impedance spectroscopy (EIS; Figure 4d). The semicircle in the high-to-medium frequency regime of the Nyquist plot was assigned to the charge-transfer resistance between electrode and electrolyte, whereas the line inclined at 45° is the

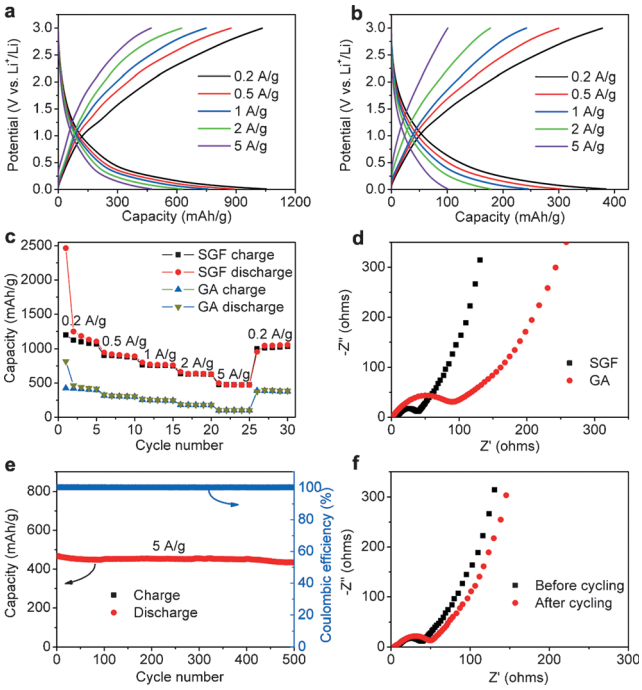

Figure 4. a, b) Galvanostatic charge/discharge profiles of SGF (a) and GA (b) electrodes. c) Rate capabilities and cycle performance of SGF and GA electrodes over a wide range of current densities from 0.2 to 5.0 $A g^{-1}$. d) Nyquist plots for SGF and GA electrodes. e) Cycling stability of the SGF electrode at a high current density of 5.0 $A g^{-1}$ after a rate performance test. The charge and discharge capacities essentially overlap with each other owing to the high Coulombic efficiency. f) Nyquist plots for the SGF electrode before and after the cycling tests.

Warburg region associated with lithium-ion diffusion in the electrode. Obviously, the SGF electrode exhibited a smaller semicircle diameter and a shorter 45° Warburg region, indicating a lower charge-transfer resistance and more efficient lithium-ion diffusion within the SGF electrode.

The SGF electrode also demonstrated excellent cycling stability in rate performance tests with a high reversible capacity of 435 $mAh g^{-1}$ and a remarkable capacity retention of 93% over 500 charge/discharge cycles at a high current density of 5.0 $A g^{-1}$ (Figure 4e). The superior structural stability of SGF was also confirmed by similar Nyquist plots before and after the cycling tests (Figure 4f), and could be attributed to the mechanically strong 3D porous network structure, which can accommodate the volume change caused by repeated lithium insertion/extraction during the cycling test. Based on the above results, the significantly improved electrochemical performance of SGF compared to GA could be attributed to its unique solvated hierarchical porous network given that the chemical structure of reduced GO in SGF and GA is identical. First, the high surface area and solvated porous structure in SGF could provide a large electrode–electrolyte interface and promote efficient and rapid lithium-ion diffusion into the entire graphene network, including the deeply buried locations within the stacked graphene layers. Second, owing to the increased intersheet distance arising from the solvation effect on the reduced GO in SGF, more active sites for lithium storage could be exposed.

We also tested the electrochemical performance of graphite as a state-of-the-art anode material for further comparison (Figure S4). The graphite material showed capacities of 326 and 121 $mAh g^{-1}$ at 0.1 and 1.0 $A g^{-1}$, respectively, which mainly comes from the lithium intercalation reaction (below 0.5 V vs. Li^+/Li), in agreement with previous results.[40] The capacities of graphite are much lower than those of the SGF electrode even considering only the capacity coming from lithium intercalation (903 and 550 $mAh g^{-1}$ at 0.1 and 1.0 $A g^{-1}$, respectively). It should also be noted that most of the previous studies on graphene-based anode materials only reported the gravimetric capacity and neglected the volumetric capacity. However, the volumetric capacity is another important metric to consider for many practical applications. Taking the packing density of the graphite anode material as approximately 2.0 $g cm^{-3}$, graphite can deliver volumetric capacities of 652 and 242 $mAh cm^{-3}$ at 0.1 and 1.0 $A g^{-1}$, respectively. With a high packing density of 0.65 $g cm^{-3}$, the SGF electrode can achieve significantly higher volumetric capacities of 753 and 487 $mAh cm^{-3}$ at 0.1 and 1.0 $A g^{-1}$, respectively. Even considering only the contribution of lithium intercalation, the SGF electrode can still show excellent volumetric capacities of 587 and 358 $mAh cm^{-3}$ at 0.1 and 1.0 $A g^{-1}$, respectively, which approach that of graphite at low current densities and greatly surpass that of graphite at high current densities. The electrochemical performance of SGF is also comparable to that of the best graphene-based anode material among a wide range of chemically modified graphene and graphene hybrids (Table S1). It is worth noting that our SGF electrode is free-standing and does not contain any other binders or additives and thus shows the highest capacity when normalized by the total weight of the entire electrode. Considering the easy large-scale and low-cost preparation as well as the lower charge/discharge potential compared to previous 3D graphene hybrids, whose capacity mainly comes from the reaction above 0.5 V (vs. Li^+/Li), the SGFs are extremely promising anode materials for LIBs with higher energy and power densities.

In summary, we have developed a convenient solvent-exchange strategy to prepare SGFs where the stacking of graphene layers and the interior microstructure within the pore walls are significantly different from those of unsolvated graphene frameworks. The SGFs can be used directly as additive-free LIB anodes and exhibit greatly improved electrochemical properties compared to unsolvated graphene frameworks, including a high reversible capacity (1158 $mAh g^{-1}$ and 753 $mAh cm^{-3}$ at 0.1 $A g^{-1}$), excellent rate capability (472 $mAh g^{-1}$ and 307 $mAh cm^{-3}$ at 5.0 $A g^{-1}$), and superior cycling stability (93% capacity retention after 500 cycles at 5.0 $A g^{-1}$). These properties are mainly due to the higher specific surface area and faster lithium-ion diffusion as well as an increased intersheet distance arising from the unique solvated porous network of SGFs. This work provides fundamental insights into the structure–property relationships of graphene frameworks, which will promote the rational design and synthesis of 3D graphene materials for electrochemical energy storage and beyond. It should also be noted that the SGF anodes show

a relatively large charge/discharge voltage hysteresis, similar to various chemically modified graphene anode materials reported previously, which will be an important topic to explore in future studies.

Experimental Section

Preparation of GO, GH, and GA: GO was prepared by oxidation of natural graphite powder according to the modified Hummers' method.[41,42] The GH was prepared using a modified hydrothermal reduction method. Briefly, an aqueous solution of ascorbic acid (0.3 mL, 1M) was added into an aqueous dispersion of GO (6 mL, 2 mg mL^{-1}), and the mixture was sealed in a Teflon-lined autoclave and maintained at 180 °C for 2 hours. The autoclave was naturally cooled to room temperature, and the as-prepared GH was taken out with tweezers and washed with water to remove residual ascorbic acid for the following experiments. GA was prepared by freeze-drying of GH using liquid nitrogen.

Preparation of the SGFs: For the preparation of SGFs with IL (1-ethyl-3-methylimidazolium tetrafluoroborate, $EMIMBF_4$), the GH was immersed in neat $EMIMBF_4$ under vacuum at 100 °C for 12 hours to exchange its interior water molecules with $EMIMBF_4$. For the preparation of SGFs with hydrophilic organic solvents, the GH was immersed in the fresh solvent with 10 times the volume under stirring for 6 hours, which was repeated three times. For the preparation of SGFs with LIB electrolyte, a piece of GH was first converted into SGF with $EMIMBF_4$; then the $EMIMBF_4$ within the SGF was further exchanged with the $LiPF_6$ EC/DEC (1M, 1:1 v/v) electrolyte. For comparison, the GA was also sequentially immersed in $EMIMBF_4$ and $LiPF_6$ EC/DEC (1M) electrolyte.

Materials characterization: The morphologies of the GHs and GAs were characterized by SEM (JEOL 6700) and TEM (FEI CM120). XRD measurements were conducted with a Panalytical X'Pert Pro X-ray Powder Diffractometer with Cu Kα radiation. The MB dye adsorption method was employed to measure the specific surface areas of HGFs and GFs. MB adsorption is a standard method for measuring the specific surface area of graphitic materials, with 1 mg of adsorbed MB molecules covering a surface area of 2.54 m^2.[39] The surface areas were calculated by adding a piece of GH or GA into a solution with a standard concentration of MB in deionized water for a total of 48 hours to completely reach the adsorption equilibrium. The MB concentration was determined by analyzing the supernatant by UV/Vis spectroscopy at a wavelength of 665 nm and a comparison to the initial standard concentration of MB prior to interacting with GH or GA. Raman spectra were measured and collected using a 632.8 nm laser with a Renishaw 1000 under ambient conditions.

Electrochemical measurements: The working electrode was prepared by direct pressing of a piece of SGF or GA with electrolyte on copper foil with 100 MPa pressure, during which the squeezed electrolytes were removed with filter papers. The mass loading of graphene was ca. 2 mg cm^{-2}. To determine the packing density of the SGF electrode, we calculated the volume (V) by measuring the radius (r) and thickness (h) of the pressed SGF film ($V = h\pi r^2$), and directly weighed the net mass of the dried SGF film after removal of interior electrolyte by repeated washing. We thus obtained the packing density by dividing the net mass by the volume of the SGF film. The graphite electrode was prepared by mixing graphite powder (95 wt%) and poly(vinylidene fluoride) binder (5 wt%) in *N*-methyl-2-pyrrolidinone and coating the above mixture slurry on a copper foil, which was followed by vacuum drying at 120 °C and pressing. The mass loading of graphite was ca. 2 mg cm^{-2}. The Li/SGF cells were assembled in an argon-filled glovebox with less than 1 ppm of oxygen and water, using lithium metal as the counter/reference electrode, a Celgard 2400 membrane separator, and $LiPF_6$ electrolyte solution (1M) dissolved in a mixture of EC and DEC (1:1 v/v). CR2032 (3 V) coin-type cells were used for electrochemical measurements. All of the electrochemical experiments were carried out using VersaSTAT 4 from Princeton Applied Research. Galvanostatic charge/discharge cycles were measured at various current densities of 0.1–5.0 A g^{-1} between 3.0 and 0.01 V versus Li^+/Li at room temperature. EIS studies were carried out at open-circuit potential with a sinusoidal signal over a frequency range from 100 kHz to 10 mHz at an amplitude of 10 mV.

Keywords: anodes · electrochemistry · graphene · lithium-ion batteries · porous materials

How to cite: *Angew. Chem. Int. Ed.* **2015**, *54*, 5345–5350
Angew. Chem. **2015**, *127*, 5435–5440

[1] M. S. Whittingham, *Proc. IEEE* **2012**, *100*, 1518–1534.
[2] N. Armaroli, V. Balzani, *Energy Environ. Sci.* **2011**, *4*, 3193–3222.
[3] A. S. Aricò, P. Bruce, B. Scrosati, J. Tarascon, W. V. Schalkwijk, *Nat. Mater.* **2005**, *4*, 366–377.
[4] Y. Q. Sun, Q. Wu, G. Q. Shi, *Energy Environ. Sci.* **2011**, *4*, 1113–1132.
[5] Z. S. Wu, G. M. Zhou, L. C. Yin, W. Cai, F. Li, H. M. Cheng, *Nano Energy* **2012**, *1*, 107–131.
[6] S. Han, D. Q. Wu, S. Li, F. Zhang, X. L. Feng, *Small* **2013**, *9*, 1173–1187.
[7] E. Yoo, J. Kim, E. Hosono, H. Zhou, T. Kudo, I. Honma, *Nano Lett.* **2008**, *8*, 2277–2282.
[8] D. Pan, S. Wang, B. Zhao, M. Wu, H. Zhang, Y. Wang, Z. Jiao, *Chem. Mater.* **2009**, *21*, 3136–3142.
[9] C. Wang, D. Li, C. O. Too, G. G. Wallace, *Chem. Mater.* **2009**, *21*, 2604–2606.
[10] X. Zhao, C. M. Harner, M. C. Kung, H. Kung, *ACS Nano* **2011**, *5*, 8739–8749.
[11] C. Li, G. Q. Shi, *Adv. Mater.* **2014**, *26*, 3992–4012.
[12] X. H. Cao, Z. Y. Yin, H. Zhang, *Energy Environ. Sci.* **2014**, *7*, 1850–1865.
[13] N. Li, Z. Chen, W. Ren, F. Li, H. M. Chen, *Proc. Natl. Acad. Sci. USA* **2012**, *109*, 17360–17365.
[14] Y. X. Xu, K. X. Sheng, C. Li, G. Q. Shi, *ACS Nano* **2010**, *4*, 4324–4330.
[15] Y. X. Xu, Z. Y. Lin, X. Q. Huang, Y. Liu, Y. Huang, X. F. Duan, *ACS Nano* **2013**, *7*, 4042–4049.
[16] Y. X. Xu, X. Q. Huang, Z. Y. Lin, X. Zhong, Y. Huang, X. F. Duan, *Nano Res.* **2013**, *6*, 65–76.
[17] Y. X. Xu, Z. Y. Lin, X. Q. Huang, Y. Wang, Y. Huang, X. F. Duan, *Adv. Mater.* **2013**, *25*, 5779–5784.
[18] Y. X. Xu, Z. Y. Lin, X. Zhong, X. Q. Huang, N. O. Weiss, Y. Huang, X. F. Duan, *Nat. Commun.* **2014**, *5*, 4554.
[19] W. F. Chen, S. Li, C. H. Chen, L. F. Yan, *Adv. Mater.* **2011**, *23*, 5679–5683.
[20] H. Y. Sun, Y. G. Liu, Y. L. Yu, M. Ahmad, D. Nan, J. Zhu, *Electrochim. Acta* **2014**, *118*, 1–9.
[21] L. Li, G. Zhou, Z. Weng, X. Y. Shan, F. Li, H. M. Cheng, *Carbon* **2014**, *67*, 500–507.
[22] X. H. Cao, B. Zheng, X. H. Rui, W. H. Shi, Q. Y. Yan, H. Zhang, *Angew. Chem. Int. Ed.* **2014**, *53*, 1404–1409; *Angew. Chem.* **2014**, *126*, 1428–1433.
[23] P. C. Lian, J. Y. Wang, D. D. Cai, L. X. Ding, Q. M. Jia, H. H. Wang, *Electrochim. Acta* **2014**, *116*, 103–108.
[24] Y. J. Gong, S. B. Yang, L. Zhang, L. L. Ma, R. Vajtai, P. M. Ajayan, *Adv. Funct. Mater.* **2014**, *24*, 125–130.
[25] J. S. Luo, J. L. Liu, Z. Y. Zeng, C. F. Ng, L. J. Ma, H. Zhang, J. Y. Lin, Z. X. Shen, H. J. Fan, *Nano Lett.* **2013**, *13*, 6136–6143.
[26] X. Cao, Y. Shi, W. Shi, X. Rui, Q. Yan, J. Kong, H. Zhang, *Small* **2013**, *9*, 3433–3438.
[27] X. Jiang, X. L. Yang, Y. H. Zhu, J. H. Shen, K. C. Fan, C. Z. Li, *J. Power Sources* **2013**, *237*, 178–186.

[28] L. Xiao, D. Q. Wu, S. Han, Y. S. Huang, S. Li, M. Z. He, F. Zhang, X. L. Feng, *ACS Appl. Mater. Interfaces* **2013**, *5*, 3764 – 3769.
[29] Y. H. Chang, J. Li, B. Wang, H. Luo, H. Y. He, Q. Song, L. J. Zhi, *J. Mater. Chem. A* **2013**, *1*, 14658 – 14665.
[30] W. Wei, S. B. Yang, H. X. Zhou, I. Lieberwirth, X. L. Feng, K. Müllen, *Adv. Mater.* **2013**, *25*, 2909 – 2914.
[31] M. Zhang, Y. Wang, M. Q. Jia, *Electrochim. Acta* **2014**, *129*, 425 – 432.
[32] Y. S. Huang, D. Q. Wu, J. Z. Wang, S. Han, L. Lv, F. Zhang, X. L. Feng, *Small* **2014**, *10*, 2226 – 2232.
[33] R. H. Wang, C. H. Xu, M. Du, J. Sun, L. Gao, P. Zhang, H. L. Yao, C. C. Lin, *Small* **2014**, *10*, 2260 – 2269.
[34] J. Qin, C. N. He, N. Q. Zhao, Z. Y. Wang, C. S. Shi, E. Z. Liu, J. J. Li, *ACS Nano* **2014**, *8*, 1728 – 1738.
[35] R. J. Chen, T. Zhao, W. P. Wu, F. Wu, L. Li, J. Qian, R. Xu, H. M. Wu, H. M. Albishri, A. S. Al-Bogami, D. A. El-Hady, J. Lu, K. Amine, *Nano Lett.* **2014**, *14*, 5899 – 5904.
[36] Y. X. Xu, H. Bai, W. G. Lu, C. Li, G. Q. Shi, *J. Am. Chem. Soc.* **2008**, *130*, 5856 – 5857.
[37] X. Yang, J. Zhu, L. Qiu, D. Li, *Adv. Mater.* **2011**, *23*, 2833 – 2838.
[38] X. Yang, L. Qiu, C. Cheng, Y. Wu, Z. F. Ma, D. Li, *Angew. Chem. Int. Ed.* **2011**, *50*, 7325 – 7328; *Angew. Chem.* **2011**, *123*, 7463 – 7466.
[39] M. J. McAllister, J. L. Li, D. H. Adamson, H. C. Schniepp, A. A. Abdala, J. Liu, M. H. Alonso, D. L. Milius, R. Car, R. K. Prud'homme, I. A. Aksay, *Chem. Mater.* **2007**, *19*, 4396 – 4404.
[40] J. Zhang, H. Cao, X. Tan, W. Fan, G. Peng, M. Qu, *J. Power Sources* **2013**, *241*, 619 – 626.
[41] W. S. Hummers, R. E. Offeman, *J. Am. Chem. Soc.* **1958**, *80*, 1339.
[42] Y. X. Xu, L. Zhao, H. Bai, W. J. Hong, C. Li, G. Q. Shi, *J. Am. Chem. Soc.* **2009**, *131*, 13490 – 13497.

Received: January 23, 2015
Published online: March 10, 2015

